AIChE

Volume-of-Fluid-Based Model for Multiphase Flow in High-Pressure Trickle-Bed Reactor: Optimization of Numerical Parameters

Rodrigo J. G. Lopes and Rosa M. Quinta-Ferreira
GERSE—Group on Environmental, Reaction and Separation Engineering, Dept. of Chemical Engineering, University of Coimbra, Rua Sílvio Lima, Polo II–Pinhal de Marrocos, 3030-790 Coimbra, Portugal

DOI 10.1002/aic.11862
Published online August 28, 2009 in Wiley InterScience (www.interscience.wiley.com).

Aiming to understand the effect of various parameters such as liquid velocity, surface tension, and wetting phenomena, a Volume-of-Fluid (VOF) model was developed to simulate the multiphase flow in high-pressure trickle-bed reactor (TBR). As the accuracy of the simulation is largely dependent on mesh density, different mesh sizes were compared for the hydrodynamic validation of the multiphase flow model. Several model solution parameters comprising different time steps, convergence criteria and discretization schemes were examined to establish model parametric independency results. High-order differencing schemes were found to agree better with the experimental data from the literature given that its formulation includes inherently the minimization of artificial numerical dissipation. The optimum values for the numerical solution parameters were then used to evaluate the hydrodynamic predictions at high-pressure demonstrating the significant influence of the gas flow rate mainly on liquid holdup rather than on two-phase pressure drop and exhibiting hysteresis in both hydrodynamic parameters. Afterwards, the VOF model was applied to evaluate successive radial planes of liquid volume fraction at different packed bed cross-sections.
 AIChE J, 55: 2920–2933, 2009
Keywords: computational fluid dynamics, trickle-bed reactor, VOF model, multiphase flow, liquid holdup, pressure drop

Introduction

Trickle-bed reactors are catalytic fixed-bed tubular devices in which a gas–liquid stream flows vertically downwards. Industrial applications arise traditionally in petrochemical and chemical industries, in biochemical, and electrochemical processing and more recently in waste gas and wastewater treatment. Well-known hydrodynamic issues are often related with partial particle-scale external wetting also referred as wetting efficiency that can cause inefficient catalyst utilization and poor heat and mass transfer rates. This hydrodynamic parameter is calculated from the percentage of external wetted surface area divided by the total solid particles surface area, and it is critical in setting the proper reactor operating specifications in order to maximize and promote higher conversion rates.[1,2] In case of exothermic reactions, partial wetting can indeed lead to poor catalyst wetting effectiveness factors and poor heat withdrawal. To ensure full coverage with a continuous liquid film of all pellets in the bed, it is necessary to guarantee a sufficient gas and liquid feeding.

The scaleup/down and design of laboratorial and commercial trickle-bed reactors depends heavily on the specific knowledge of two-phase pressure drop, liquid holdup and the catalyst wetting efficiency as a function of operating conditions and the mathematical formulation derived is frequently

Correspondence concerning this article should be addressed to R. M. Quinta-Ferreira at rosaqf@eq.uc.pt

system specific and it is feasible only in a particular range of operation in which the correlation was obtained. Recently, computational fluid dynamics (CFD) appeared as a promising tool to understand the complex hydrodynamics in more detail requiring closure laws for the interphase coupling forces in the momentum balance equation-based on the Eulerian-Eulerian approach.[3,4] However, this mathematical treatment is incapable to capture the wetting features as well as the so-called hysteresis in the operation of trickle beds reviewed by Nigam et al.[5] and Saroha et al.[6]

The simulation of gas–liquid–solid interfaces of a multiphase flow is still under investigation presenting a computational challenge in CFD despite the advancements already achieved. Known issues are related with the exact location of the interface, calculation of surface tension, and the high dissimilarity of fluid properties. For a water/air system the variation can be three orders of magnitude and the numerical method should be capable of maintaining a sharp interface without stretching it over a couple of cells due to numerical diffusion.

Therefore, it is of paramount importance to formulate a detailed CFD model that can capture the microscale interaction processes between both surfaces. Our attempt is to supply a deep understanding of fluid hydrodynamics parameters through the development of a Volume-of-Fluid-based computational fluid model for simulating the gas–liquid surface.

There are two different classes of methods to deal with the surface modeling techniques: tracking and capturing methods. Front tracking, boundary integral, moving mesh and particle schemes are tracking methods because they are of Lagrangian type, in which the interface position is identified by a particle or a polygon called a Lagrangian marker. Alternatively, level set, continuum advection, volume tracking and phase field method schemes are capturing type methods.[7]

Several literature studies on wetting dynamics[8–10] considered high velocities (in the range 1–6 m/s), however in trickle bed reactors, the liquid phase interacts with the catalyst solid surface with substantially lower velocities. In the theoretical field, recent works were published on the numerical simulation of gas–liquid flows by means of a VOF model. Yuan et al.[11] applied a VOF method based on a piecewise linear interface construction (PLIC) to track the liquid–vapor interface in the simulation of natural convection film boiling and forced convection film boiling on a sphere at saturated conditions. Glatzel et al.[12] evaluated the performance of commercial CFD codes based on VOF method when applied as and engineering tool for microfluidic applications. Surface tension effects and flow patterning of two fluids were studied in terms of computational speed and comparison with experimental data. Gopala et al.[13] analyzed a number of numerical methods to track interfaces in multiphase flows including the level-set method, the marker particle method and the front tracking method. The authors concluded that the VOF method has an advantage of being conceptually simple, reasonably accurate and phenomena such as interface breakup and coalescence are inherently included. Morel[14] presented alternative modeling approaches for strongly nonhomogeneous two-phase flows in where the flow domain is divided into a bubbly region and a droplet region separated by a free surface. The closure problem is discussed for each model and the three models are compared according to several criteria. Heggemann et al.[15] modeled the fluid flow in liquid distributors and the validation was accomplished in the uniform distribution of liquid above structured packings for its performance prediction.

None of the VOF models published in the literature were used to simulate the trickling flow or even the spraying and pulsing hydrodynamic regimes in TBRs. Taking into account the large number of studies that were carried out for measurement of pressure drop and liquid holdup in trickle beds[1,16,17] a limited number can only be found which addressed the effect of prewetted and nonprewetted bed conditions on two-phase pressure drop and liquid holdup including the respective hysteresis. Kan and Greenfield explained the hysteresis phenomenon based on the formation of liquid bridges and surface tension.[18,19] Christensen et al.[20] and Levec et al.[21,22] observed that the radial distribution of the liquid in the bed changes depending on whether the liquid flow rate increases or decreases and stated it as a cause for hysteresis. Rode et al.[23] have also reported multiple hydrodynamics states in various flow regimes of trickle-bed reactors. Ravindra et al.[24] presented experimental data on hysteresis while Melli and Scriven[25] studied hysteresis theoretically in a two-dimensional bed. Recently, Gunjal et al.[4] modeled the hysteresis in pressure drop and liquid holdup by means of an Eulerian framework.

The present VOF model was undertaken to simulate the wetting phenomena in high-pressure (30 bar) trickle-bed reactors providing a better understanding of its liquid distribution and hysteresis. The hydrodynamic validation is accomplished in terms of pressure drop and liquid holdup experimental data taken from the open literature and afterwards, computational predictions for the wetting efficiency will be investigated at different liquid flow rates.

CFD Modeling

Volume fraction equation

The VOF method was used to compute phase volume fractions as well as velocity field maps. The multiphase flow is assumed to be vertical downward and incompressible, with the mathematical description for the flow of a viscous fluid through a three-dimensional catalytic bed based on a single set of momentum equations and tracking the volume fraction of each of the fluids throughout the domain. Taking into account that packed bed flow is often described in transient mode, so the present VOF formulation was used to compute a time-dependent solution. The volume fraction of the phase q in the computational cell is specified for each one of the phases as α_q. In each control volume, the volume fractions of all phases sum to unity and the fields for all variables and properties are shared by the phases and represent volume-averaged values, as long as the volume fraction of each of the phases is known at each location. Thus, the variables and properties in any given cell are either purely representative of one of the phases, or representative of a mixture of the phases, depending upon the volume fraction values: if the qth fluid's volume fraction in the cell is denoted as α_q, then the following three conditions are possible: $\alpha_q = 0$: the cell is empty of the qth fluid; $\alpha_q = 1$: the cell is full of the

qth fluid; $0 < \alpha_q < 1$: the cell contains the interface between the both fluid phases. Based on the local value of α_q, the appropriate properties and variables will be assigned to each control volume within the domain.

The tracking of the interface between the phases is accomplished by the solution of a continuity equation for the volume fraction of one (or more) of the phases. For the qth phase, this equation has the following form of Eq. 1.

$$\frac{1}{\rho_q}\left[\frac{\partial}{\partial t}\left(\alpha_q\rho_q\right) + \nabla.\left(\alpha_q\rho_q\vec{v}_q\right) = S_{\alpha_q} + \sum_{p=1}^{n}\left(\dot{m}_{pq} - \dot{m}_{qp}\right)\right] \quad (1)$$

where $\dot{m}_{pq}$ is the mass transfer from phase q to phase p and $\dot{m}_{qp}$ is the mass transfer from phase p to phase q. The source term on the right-hand side of Eq. 1, S_{α_q}, is used to compute the mass source for each phase. The primary-phase volume fraction was computed based on the following constraint:

$$\sum_{q=1}^{n}\alpha_q = 1 \quad (2)$$

Momentum equation

A single momentum equation is solved throughout the computational domain, and the resulting velocity field is shared among the phases. The momentum equation, shown below in Eq. 3, is dependent on the volume fractions of all phases through the properties ρ and μ.

$$\frac{\partial}{\partial t}(\rho\vec{v}) + \nabla\cdot(\rho\vec{v}\vec{v}) = -\nabla p + \nabla\cdot\left[\mu\left(\nabla\vec{v} + \nabla\vec{v}^T\right)\right] + \rho\vec{g} + \vec{F} \quad (3)$$

One limitation of the shared-fields approximation is that in cases where large velocity differences exist between the phases, the accuracy of the velocities computed near the interface can be adversely affected. A viscosity ratio more than 10^3 may also lead to convergence difficulties so that the compressive interface capturing scheme for arbitrary meshes was evaluated throughout the TBR modeling.

Surface tension

The VOF model includes the effects of surface tension along the interface between each pair of phases and the additional specification of the contact angles between the phases and the walls.[26] Surface tension arises as a result of attractive forces between molecules in a fluid. At the surface between air and water, the net force is radially inward, and the combined effect of the radial components of force across the entire surface is to make the surface contract, thereby increasing the pressure on the concave side of the surface. The surface tension is a force, acting only at the surface that is required to maintain equilibrium in such instances. It acts to balance the radially inward inter-molecular attractive force with the radially outward pressure gradient force across the surface. In regions where two fluids are separated, the surface tension acts to minimize free energy by decreasing the area of the interface. The surface tension is modeled by means of the continuum surface force (CSF) model proposed by Brackbill et al.[27] With this model, the addition of surface tension to the VOF calculation results in a source term in the momentum equation. In the case of constant surface tension along the surface and considering only the forces normal to the interface, the pressure drop across the surface depends upon the surface tension coefficient, σ, and the surface curvature as measured by two radii in orthogonal directions, R_1 and R_2, as expressed in Eq. 4.

$$p_2 - p_1 = \sigma\left(\frac{1}{R_1} + \frac{1}{R_2}\right) \quad (4)$$

where p_1 and p_2 are the pressures in the two fluids on either side of the interface. In the formulation of the CSF model, the surface curvature is computed from local gradients in the surface normal at the interface. Let n be the surface normal, defined in Eq. 5 as the gradient of α_q, the volume fraction of the qth phase.

$$n = \nabla\alpha_q \quad (5)$$

The curvature, κ, is defined in Eq. 6 in terms of the divergence of the unit normal,[27] $\hat{n}$:

$$\kappa = \nabla\cdot\hat{n} \quad (6)$$

where

$$\hat{n} = \frac{n}{|n|} \quad (7)$$

The surface tension is expressed in terms of the pressure jump across the surface. The force at the surface can be expressed as a volume force using the divergence theorem. It is this volume force that is the source term which is added to the momentum equation and has the following form:

$$F_{\text{vol}} = \sum_{\text{parts } ij,\, i<j}\sigma_{ij}\frac{\alpha_i\rho_i\kappa_j\nabla\alpha_j + \alpha_j\rho_j\kappa_i\nabla\alpha_i}{\frac{1}{2}\left(\rho_i + \rho_j\right)} \quad (8)$$

Equation 8 allows for a smooth superposition of forces near cells where more than two phases are present. If only two phases are present in a cell, then $\kappa_i = -\kappa_j$ and $\bigtriangledown\alpha_i = -\bigtriangledown\alpha_j$, this equation simplifies to Eq. 9.

$$F_{\text{vol}} = \sigma_{ij}\frac{\rho\kappa_i\nabla\alpha_i}{\frac{1}{2}\left(\rho_i + \rho_j\right)} \quad (9)$$

where ρ is the volume-averaged density computed using equation: $\rho = \sum\alpha_q\rho_q$.

The importance of surface tension effects is determined based on the value of two dimensionless quantities: the Reynolds number, Re, and the capillary number, Ca; or the Reynolds number, Re, and the Weber number, We. For $Re \ll 1$, the quantity of interest is the capillary number given by Eq. 10.

$$Ca = \frac{\mu v}{\sigma} \quad (10)$$

and for $Re \gg 1$, the quantity of interest is the Weber number as shown in Eq. 11.

$$We = \frac{\rho L v^2}{\sigma} \tag{11}$$

where v is the free-stream velocity. Surface tension effects can be neglected if $Ca \gg 1$ or $We \gg 1$.

Wall adhesion

To specify wall adhesion angle in conjunction with the surface tension model, the VOF model taken from work done by Brackbill et al.[27] was also investigated. Rather than impose this boundary condition at the wall itself, the contact angle that the fluid is assumed to make with the wall is used to adjust the surface normal in cells near the wall. If θ_w is the contact angle at the wall, then the surface normal at the live cell next to the wall is given by Eq. 12.

$$\hat{n} = \hat{n}_w \cos\theta_w + \hat{t}_w \sin\theta_w \tag{12}$$

where $\hat{n}_w$ and $\hat{t}_w$ are the unit vectors normal and tangential to the wall, respectively. The combination of this contact angle with the usually calculated surface normal one cell away from the wall determine the local curvature of the surface, and this curvature is used to adjust the body force term in the surface tension calculation.

Turbulence modeling

Trickle-beds are mostly operated at low interaction regimes so that the flow is often assumed laminar either at the reactor level or at the catalyst particle scale. However, several studies have looked at the transition to turbulence, the level of turbulence intensity in the void space, and the description of flow regimes in fixed bed flow. Dybbs et al.[28] used laser anemometry and flow visualization to study flow regimes of liquids in hexagonal packings of spheres and rods and concluded that there are four flow regimes for different ranges of Reynolds number, based on interstitial or pore velocity $Re_i = Re/\varepsilon$: for $Re_i < 1$, the creeping flow is dominated by viscous forces and pressure drop is linearly proportional to interstitial velocity; for $1 \leq Re_i \leq 150$, the steady laminar inertial flow in which pressure drop depends nonlinearly on interstitial velocity; for $150 \leq Re_i \leq 300$, the laminar inertial flow is unsteady; and for $Re_i > 300$, the flow is highly unsteady, chaotic and qualitatively resembling turbulent flow. Likewise, Gunjal et al.[26] used a laminar model up to $Re_i = 204$ and turbulent models for $Re_i = 1{,}000$–$2{,}000$. Therefore, since the Reynolds numbers range for the gas phase is wide (min: 10, max: 2500), a k-ε model was applied for turbulence modeling.[29,30]

The turbulence kinetic energy, k, and the turbulent dissipation rate, ε, are computed from Eqs. 13 and 14.

$$\frac{\partial}{\partial t}(\rho_m k) + \nabla \cdot (\rho_m \vec{u}_m k) = \nabla \cdot \left(\frac{\mu_{t,m}}{\sigma_k} \nabla k\right) + G_{k,m} - \rho_m \varepsilon \tag{13}$$

$$\frac{\partial}{\partial t}(\rho_m \varepsilon) + \nabla \cdot (\rho_m \vec{u}_m \varepsilon) = \nabla \cdot \left(\frac{\mu_{t,m}}{\sigma_\varepsilon} \nabla \varepsilon\right) + \frac{\varepsilon_m}{k_m} \times \left(C_{1\varepsilon} G_{k,m} - C_{2\varepsilon} \rho_m \varepsilon\right) \tag{14}$$

and the production of turbulence kinetic energy, $G_{k,m}$, is computed from Eq. 15.

$$G_{k,m} = \mu_{t,m}\left(\nabla \vec{u}_m + (\nabla \vec{u}_m)^T\right) : \nabla \vec{u}_m \tag{15}$$

$C_{1\varepsilon}$ and $C_{2\varepsilon}$ are the constants of standard k-ε model whereas σ_k and σ_ε are the turbulent Prandtl numbers for k and ε, respectively.

Numerical Simulation

Trickle-bed geometry, fluid properties, operating, and boundary conditions

The present case-study encompasses a trickle-bed reactor that was designed using regular shape catalyst particles for multifluid Eulerian simulations.[31] Gas-liquid flows through a catalytic bed comprised of monosized, spherical, solid particles arranged in a cylindrical container of a pilot TBR unit (50 mm internal diameter $\times$1.0 m length). The computational mesh of the catalytic bed was shortened in length given the high memory requirements so that the reactor was filled with 10 layers in which around 200 nonoverlapping spherical particles of 2-mm diameter were necessary for each axial layer as shown in Figure 1. To prevent numerical difficulties associated with the mesh generation also reported in the literature,[32] the catalyst particles do not touch each other and the distance gap was fixed by 2–3 % percent of the sphere diameter. The grid of catalytic bed was created using the integrated solid modeling and meshing commercial program GAMBIT.[33] Geometrical errors arising from the mesh style and quality were evaluated according to different mesh densities and discretization parameters. Consecutively, the number of cells necessary to produce grid independent results for the hydrodynamic parameters was increased from

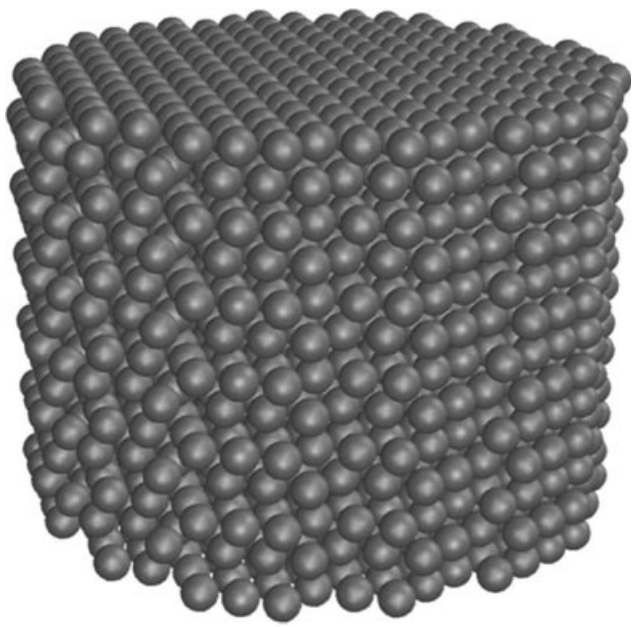

Figure 1. Scheme of the catalytic packing geometry for the trickle-bed reactor.

Table 1. Numerical Solution Parameters Used in the CFD Simulation

Grid	1000 mm (axial) × 50 mm (radial)
Cell size	0.05–0.20 mm (tetrahedral cells)
Particle diameter	2 mm (spheres)
Time step (s)	10^{-7} to 10^{-2}
Convergence criteria (s)	10^{-6} to 10^{-3}
Discretization method	QUICK, Geo-Reconstruct, CICSAM and HRIC
Iterations	≈50,000
Under-relaxation parameters	VOF: 0.4 (pressure), 0.6 (velocity)
Drag formulation	Brackbill et al., 1992[27]
Turbulence model	k-ε model (Elghobashi et al., 1984)[29]

2×10^5 to 10^6, with other numerical solution parameters including operating conditions given by Table 1.

Gas and liquid thermophysical properties used in the simulation are summarized in Table 2. High-pressure operation was simulated at 30 bar total operating pressure with inflow gas ($G = 0.1$–0.7 kg/m^{2}s) and liquid ($L = 1$–15 kg/m^{2}s) being distributed uniformly with given superficial velocity replicating a uniform distributor at the top of a trickle-bed reactor.

The boundary conditions were specified based on FLUENT documentation.[30] Inlet turbulent kinetic energy (k) was estimated from turbulence intensity as expressed in Eq. 16.

$$k = \frac{3}{2}(uI)^2 \tag{16}$$

where I is the turbulence intensity being given by Eq. 17.

$$I = 0.16(Re_{d_H})^{-1/8} \tag{17}$$

Inlet turbulent dissipation rate (ε) was estimated from the turbulent viscosity ratio as expressed by Eq. 18.

$$\varepsilon = \rho C_\mu \frac{k^2}{\mu}\left(\frac{\mu_t}{\mu}\right)^{-1} \tag{18}$$

where C_μ is an empirical constant specified in the turbulence model (0.09). At 30 bar and 25°C, the inlet turbulent kinetic energy and inlet turbulent dissipation rate for the gas and liquid phases are given in Tables 3 and 4. Computations are time dependent and were carried out until steady state conditions were reached. In case of turbulent flow, standard wall functions were employed available in the commercial CFD solver. Although FLUENT documentation recommends a range of 30–50 for the cell thickness (y^+), in packed-bed flow it is almost impossible the meet the $y+$ criterion everywhere on the sphere surface so that this value computed by the CFD solver was always less than 200. The calculations have been carried out on a Linux cluster based on AMD64 Dual-Core 2.2 GHz processor workstation.

Table 2. Relevant Thermophysical Properties of Gas and Liquid Phases

	Value ($P = 30$ bar)		
Properties	$T_1 = 25$°C	$T_1 = 200$°C	Units
Liquid phase			
Viscosity	8.925×10^{-4}	1.340×10^{-4}	Pa s
Density	998.4	866.9	kg/m^3
Surface tension	7.284×10^{-2}	3.770×10^{-2}	N m
Gas phase			
Viscosity	1.845×10^{-5}	2.584×10^{-5}	Pa s
Density	35.67	21.97	kg/m^3

Table 3. Inlet Boundary Conditions for the Gas Phase: Turbulent Kinetic Energy (k_i) and Turbulent Dissipation Rate (ε_i) at $P = 30$ Bar

G (kg/m^{2}s)	k_G (mm^2/s^2)	ε_G (mm^2/s^3)
0.1	0.2059	3.690×10^{-3}
0.4	2.330	0.4723
0.7	6.204	3.349

Results and Discussion

Mesh size optimization

The liquid holdup and pressure drop predicted by the CFD simulations are quantitatively compared with the literature experimental results[1,34] for different mesh densities. In Figure 2, the liquid holdup predictions are plotted as a function of liquid flow rate at $P = 30$ bar and $G = 0.1$ kg/m^{2}s with different mesh resolutions. This criterion was based on the number of tetrahedral cells needed to achieve a grid independent solution. The routine procedure was as follows: at a given liquid flow rate, the flow domain was initialized for a fixed number of cells and after reaching the steady-state solution, the liquid holdup value was used to build the hydrodynamic profile shown in Figure 2. This procedure was replicated increasing the number of tetrahedral cells until the asymptotic value for liquid holdup was found. This iterative method is accomplished for different liquid flow rates in the range 2–15 kg/m^{2}s. The coarsest mesh corresponds to about 2×10^5 of tetrahedral cells and the finest mesh had about 1 million of tetrahedral cells. Depending on the geometric configuration of the catalytic bed, the average cell size is in the range 0.05–0.2 mm which gives a spatial resolution less than $d_p/20$, for the finer meshes. It is worth noting that this cell size was determined after the gap imposition between the catalyst particles of 2 mm that is needed to prevent the loss of numerical accuracy but simultaneously it must not produce unexpected numerical diffusion errors arising in the grid generation. Furthermore, the wall functions available in the CFD solver were evaluated during grid optimization, which allowed the selection of standard wall functions throughout the TBR simulation at high-pressure operation.

Several authors have simulated heat transfer phenomena in gas-solid packed beds. Dixon et al.[32] modeled the contact points between catalyst particles with common nodes on the surfaces so that the computational cells around these contact points used two nodes on either wall to define their volume. In

Table 4. Inlet Boundary Conditions for the Liquid Phase: Turbulent Kinetic Energy (k_i) and Turbulent Dissipation Rate (ε_i) at $P = 30$ Bar

L (kg/m^{2}s)	k_L (mm^2/s^2)	ε_L (mm^2/s^3)
1	3.952×10^{-2}	7.637×10^{-5}
8	1.504	0.1106
15	4.518	0.9982

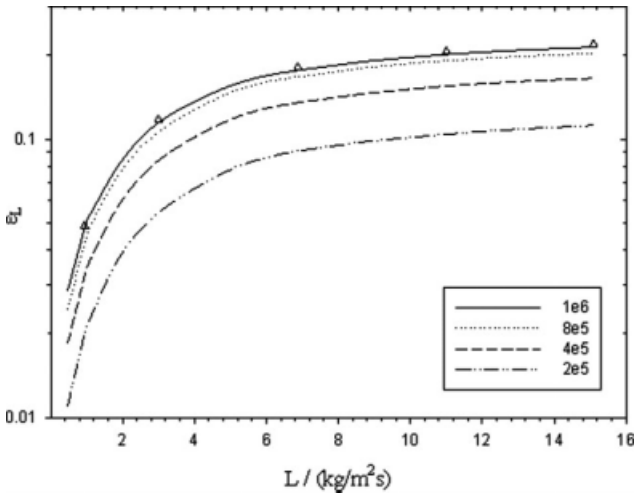

Figure 2. Comparison of liquid holdup predictions as a function of liquid flow rate for different number of cells (G = 0.1 kg/m^{2}s, P = 30 bar, d_p = 2 mm and experimental data from Nemec and Levec, 2005).[34]

our TBR mesh, this procedure created noteworthy skewed cells which mean that surfaces were much larger than others within the one tetrahedron. While in laminar flow simulations this fact did not distress convergence, for turbulent flow simulation the Reynolds stresses calculations were affected due to the fact that the flow velocities in the contact points are significant higher. Therefore, the small gap corresponds to 2–3% of catalyst diameter had to be imposed in order to prevent numerical convergence issues with skewed tetrahedral cells.

According to Figure 2, the numerical simulations performed at $L = 15$ kg/m^{2}s with the coarser meshes (2×10^5, 4×10^5) gave a relative error of 48.9 and 24.6%, while the finer meshes (8×10^5, 10^6) gave 7.4 and 2.7% of relative error, respectively. At $L = 1$ kg/m^{2}s, the relative errors for the computed liquid holdup results were 59.4, 34.4, 13.4, and 6.9%. Therefore, a optimum number of about 10^6 cells gave mesh-independent results with respect to liquid holdup. In Figure 3, the frictional pressure drop predictions are plotted as a function of liquid flow rate at high-pressure operation. At $P = 30$ bar and $L = 15$ kg/m^{2}s, the relative errors obtained for the two-phase pressure drop were 45.9, 27.1, 13.1, and 7.7% from the coarse to the fine meshes, respectively. If the operation is simulated at the lowest liquid flow rate ($L = 1$ kg/m^{2}s), the relative errors became 57.5, 34.6, 16.4, and 8.4% for 2×10^5, 4×10^5, 8×10^5, and 10^6 of tetrahedral cells, respectively. As one can conclude, both hydrodynamic parameters are underpredicted if one uses coarse meshes and the same value for the number of tetrahedral cells were achieved for mesh-independent results with respect to both liquid holdup and pressure drop so that the finest mesh was used as the base case setting for subsequent parametric investigation of other VOF modeling parameters.

Time step and convergence criterion

Since the finest grid with about 1 million of tetrahedral cells gave mesh-independent results, this mesh was used for time step studies. A nominal time step in the range 0.01–0.001 s has often been used for gas-liquid flow in the Eulerian simulations for packed-bed flows.[3,4,31] However, with the VOF model during the grid optimization several fixed time step sizes were investigated. For the coarse grid, whatever time step was being used, the numerical accuracy was not always satisfactory. Alternatively, with the fine grid, times steps of 0.001 and 0.005 s gave very similar steady state results but neither 0.005 s nor 0.001 s time steps produce the best accurate computed results close to the experimental values. Additionally, a time step of 0.001 s led to a slightly different transient behavior being the multiphase flow profiles for either pressure drop or liquid holdup more stable in time with shorter time steps rather than with higher time steps. Following the time step screening activities, its value was decreased from 0.001 s to 0.0001 s and further to 0.00001 s. In Figure 4, the liquid holdup from the numerical simulations was plotted as a function of liquid flow rate for several time steps investigated with VOF multiphase model whereas the pressure drop simulations at $P = 30$ bar are given in Figure 5 for the same tested time steps. Indeed, as long as the time step is decreased to 10^{-5} s, the hydrodynamic predictions were found to be in good agreement with experimental data. At $G = 0.1$ kg/m^{2}s and for the highest liquid flow rate simulated ($L = 15$ kg/m^{2}s), the relative errors obtained with time steps of 10^{-2}, 10^{-3}, 10^{-4}, and 10^{-5} s were 60.9, 36.5, 10.0, and 2.7% for the liquid holdup computations (Figure 4), respectively. For the case of pressure drop calculations (Figure 5), the relative errors obtained between the computed and experimental results were larger than those attained with liquid holdup remaining at 61.4, 40.7, 15.1, and 7.7% for the corresponding time steps. The time step was also decreased to 10^{-6} and 10^{-7} s, but seemingly this operation led to different dynamic behavior being almost unbearable the achievement of numerical convergence and stable solution. In fact, a time step of about 10^{-7} s can be only useful in the

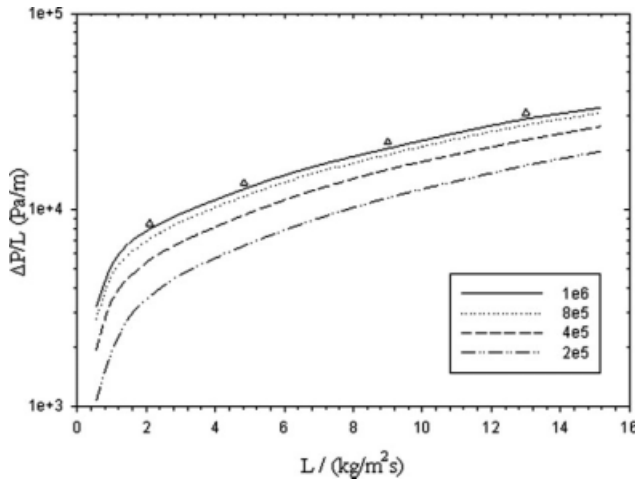

Figure 3. Comparison of two-phase pressure drop predictions as a function of liquid flow rate for different number of cells (G = 0.1 kg/m^{2}s, P = 30 bar, d_p = 2 mm and experimental data from Nemec and Levec, 2005).[34]

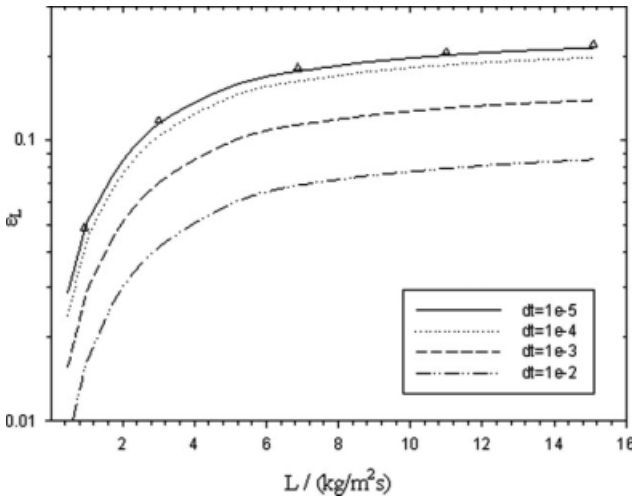

Figure 4. Effect of time step (*dt*) on liquid holdup predictions as a function of liquid flow rate with the finest mesh (10^6 of tetrahedral cells, G = 0.1 kg/m^{2}s, P = 30 bar, d_p = 2 mm and experimental data from Nemec and Levec, 2005).[34]

first iterations to promote the numerical stabilization and depending regularly on the viscosity and density ratios between the two fluid phases. Therefore, a time step of 10^{-5} s led to affordable hydrodynamic predictions for both liquid holdup and two-phase pressure drop at high-pressure being selected to generate time-step independent CFD results.

One should bear in mind that the mesh size, time step, and convergence criteria are deeply inter-related. The present case that is concerned with the multiphase flow simulation in a packed bed is heavily characterized by the unsteady-state behavior expressed directly in the computation of hydrodynamic parameters. Therefore, as the current VOF formulation was performed in transient mode, the CFD model predicted cell properties one step at a time and converges them by an iterative procedure until a specified convergence criterion is satisfied. As long as the time step becomes smaller, the predicted change of liquid holdup (or pressure drop) in a specific cell between two consecutive temporal iterations may become smaller than a fixed convergence criterion which gives a larger overall error. Consequently, the selection of time step too small as 10^{-7} s or even less had a negative impact on the simulation accuracy and the relative error became higher. However, if the time step is too large as 10^{-2} s, it gave at all less accurate hydrodynamic results. The calculation of a cell property between two temporal iterations also depends on the tetrahedral cell sizes as observed in Figures 2 and 3. For the TBR time-dependent VOF calculations, the time step used for the volume fraction calculation may not be the same as the time step used for the rest of the transport equations so that a maximum Courant number (N_c) of 0.25 was used in the VOF simulations. The dimensionless Courant number compares the time step in a calculation to the characteristic time of transit of a fluid element across a control volume as expressed in Eq. 19. In this case, based on the Courant-Friedrichs-Lewy condition (CFL) the time step was chosen to be at most one-fourth the minimum transit time for any cell near the interface.

$$N_c = \frac{\Delta t}{\Delta x_{cell}/u_{fluid}} \tag{19}$$

In Figure 6 is was plotted the liquid holdup predictions as a function of liquid flow rate with different convergence criteria for the scaled residual component of mass, velocity, etc. variables at P = 30 bar. This numerical solution parameter was not found to have the same influence than the effect of time step or mesh size. At L = 15 kg/m^{2}s, the convergence criteria of 10^{-3} which corresponds to the default value in the CFD solver gave a relative error of 15.8% for the liquid holdup computation whereas with convergence criteria of 10^{-6}, 10^{-5}, and 10^{-4} the relative errors were 2.7, 5.7, and 9.6%, respectively. As expected, a stricter convergence criterion that implied a more accurate calculations gave a better concordance with the experimental data.[1,34] This fact was also identified for the two-phase pressure drop simulations (Figure 7) with the following decreasing order of relative error achieved at L = 15 kg/m^{2}s: 7.7, 10.7, 18.9, and 28.3 for the 10^{-6}, 10^{-5}, 10^{-4}, and 10^{-3} convergence criteria.

VOF differencing scheme

After the establishment of base case settings to produce either mesh-independent or time step-independent CFD results with respect to liquid holdup and two-phase pressure drop, the finest mesh of about 1 million of cells and a time step of 10^{-5} s were used to perform additional studies on the discretization scheme of the volume fraction equation. Since high order discretization schemes are generally able to capture more realistic physical behavior, several discretization methods were investigated including the Quadratic Upwind Interpolation for Convective Kinematics (QUICK), Compressive Interface Capturing Scheme for Arbitrary Meshes (CICSAM) and High-Resolution Interface Capturing (HRIC) schemes (see Appendix).

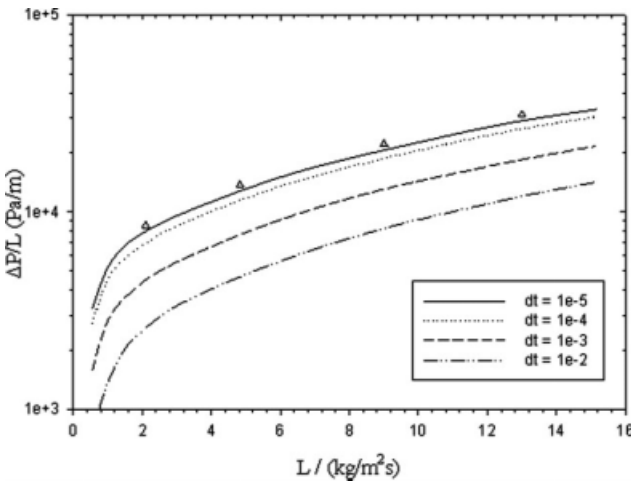

Figure 5. Effect of time step (*dt*) on two-phase pressure drop predictions as a function of liquid flow rate with the finest mesh (10^6 of tetrahedral cells, G = 0.1 kg/m^{2}s, P = 30 bar, d_p = 2 mm and experimental data from Nemec and Levec, 2005).[34]

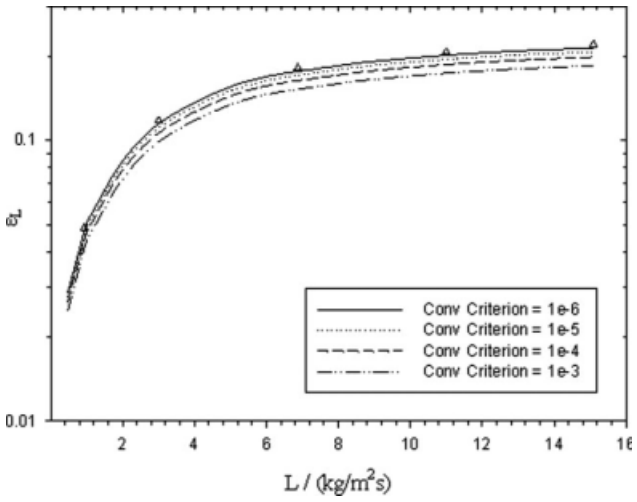

Figure 6. Effect of convergence criteria on liquid holdup predictions as a function of liquid flow rate (time step = 10^{-5} s, 10^6 of tetrahedral cells, G = 0.1 kg/m^{2}s, P = 30 bar, d_p = 2 mm and experimental data from Nemec and Levec, 2005).[34]

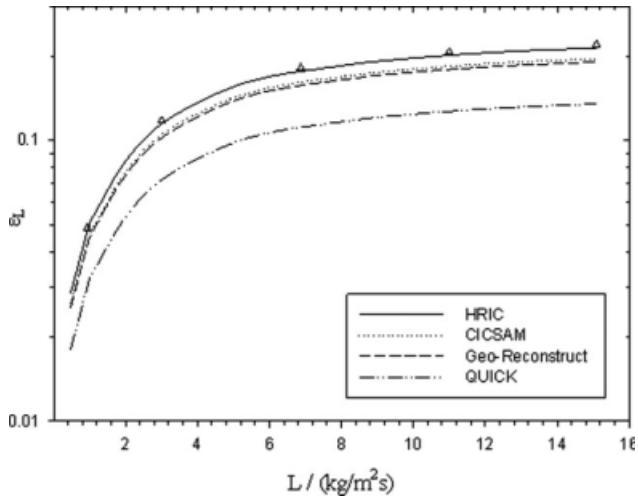

Figure 8. Effect of discretization scheme of volume fraction equation (QUICK, GR, CICSAM, and HRIC) on liquid holdup predictions as a function of liquid flow rate (time step = 10^{-5} s, 10^6 of tetrahedral cells, G = 0.1 kg/m^{2}s, P = 30 bar, d_p = 2 mm and experimental data from Nemec and Levec, 2005).[34]

In Figure 8 the predicted liquid holdup was plotted as a function of liquid flow rate with the above differencing schemes at $G = 0.1$ kg/m^{2}s and $P = 30$ bar. According to Figure 8, the calculated relative errors between the computed and experimental liquid holdup results at $L = 15$ kg/m^{2}s were 38.4, 13.2, 10.9, and 2.7% for the QUICK, GR, CICSAM and HRIC schemes, respectively. Therefore, QUICK discretization scheme was found to give the worst concordance between CFD predictions and experimental data whilst the high-order differencing schemes (CICSAM, HRIC) were found to produce reasonably accurate results and thus solving the problem of poor convergence verified with QUICK scheme.

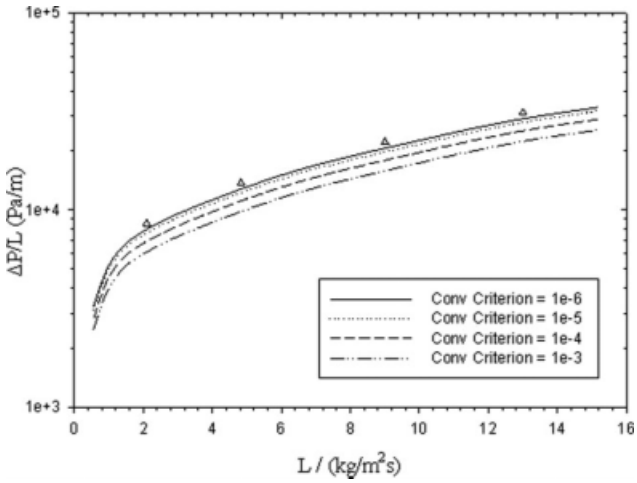

Figure 7. Effect of convergence criteria on two-phase pressure drop predictions as a function of liquid flow rate (time step = 10^{-5} s, 10^6 of tetrahedral cells, G = 0.1 kg/m^{2}s, P = 30 bar, d_p = 2 mm and experimental data from Nemec and Levec, 2005).[34]

These schemes were used to discretize the convective term in the scalar equation for the transport of the volume fraction through the computational domain. The main reason advanced for the better quantitative agreement is definitely related to its high-resolution algorithms which minimize the influence of artificial numerical dissipation and keep the shape of the step interface profile. Taking into account that upwind and central differencing schemes are known to introduce artificial diffusion or dispersion respectively to their order of accuracy, high-order schemes (mainly CICSAM and HRIC) were found to avoid these artificial numerical effects and concurrently assuring a compressive character or sharpening of the step interface profile.[35,36]

Two-phase frictional pressure drop predictions were plotted in Figure 9 as a function of liquid flow rate with the same discretization schemes at $G = 0.1$ kg/m^{2}s and $P = 30$ bar. According to Figure 9, GR scheme was found to give almost the same pressure drop results as CICSAM and HRIC. Once more, the high-order differencing schemes gave a better concordance with experimental pressure drop data and minimal relative errors. In fact, at the highest simulated liquid flow rate the relative errors were 29.8, 9.2, 8.5, and 7.7% for the QUICK, GR, CICSAM, and HRIC schemes, respectively. Hence, as the normalized variable diagram provides the mathematical foundation for both CICSAM and HRIC schemes[36] and while CICSAM is based on the convective boundedness criterion, the HRIC explicit independence on the CFL condition showed to give the best VOF multiphase predictions either for liquid holdup or pressure drop as observed in both Figures 8 and 9.

Hydrodynamics predictions

For the purpose of additional and sustainable VOF corroboration studies, several CFD simulations were carried out to

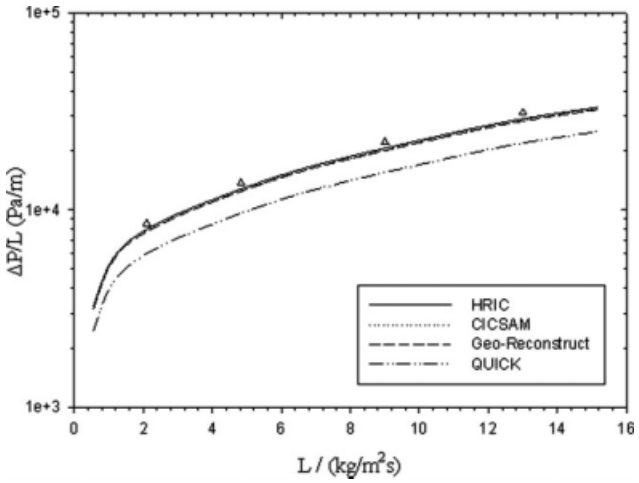

Figure 9. Effect of discretization scheme of volume fraction equation (QUICK, GR, CICSAM, and HRIC) on two-phase pressure drop predictions as a function of liquid flow rate (time step = 10^{-5} s, 10^6 of tetrahedral cells, G = 0.1 kg/m^{2}s, P = 30 bar, d_p = 2 mm and experimental data from Nemec and Levec, 2005).[34]

evaluate the effect of gas flow rate on the TBR hydrodynamics. In Figure 10, the computed liquid holdup was plotted as a function of liquid flow rate at $P = 30$ bar and adjusting the gas flow rate in the range 0.1–0.7 kg/m^{2}s. As it can be seen, two branches were obtained for a single gas flow rate. Increasing the liquid flow rate from 2 to 15 kg/m^{2}s, the computed liquid holdup corresponds to the lower profile of a nonprewetted bed while the upper profile was obtained decreasing the liquid flow rate in a prewetted catalytic bed. It is worth noting that at $G = 0.7$ kg/m^{2}s and $L = 15$ kg/m^{2}s, the prevailing hydrodynamic regime is still trickling flow according to several published flow map regimes.[1] Figure 11 shows two-phase pressure drop predictions following the same procedure as mentioned earlier at different gas flow rates. The capillary pressure acting on the solid-liquid interface is dominant for a dry catalytic bed which restricts the spreading within the bed and the liquid flows through the confined region of the bed. As expected, a larger gas–liquid interfacial interaction can be attained and the frictional pressure drop profile showed hysteresis when the liquid flow rate was decreased from 15 to 2 kg/m^{2}s. The hysteresis behavior may also depend on initial flow distribution in the catalytic bed so that an ideal gas-liquid distributor was mimicked at the top of TBR. The VOF computations for liquid holdup showed similar trends of hysteresis as those found for pressure drop which may be explained based on the formation of liquid bridges and surface tension effect.

According to Figure 10, it was found that VOF underpredicted the liquid holdup in the whole range of gas and liquid simulated flow rates. In fact, at the lowest liquid flow rate ($L = 1$ kg/m^{2}s) and varying the gas flow rate from 0.1 to 0.7 kg/m^{2}s the relative error for the computed upper liquid holdup profile were increased from 6.9 to 19.4% demonstrating that the current VOF formulation did not account the influence of gas flow rate accurately. It seems that as long as the reactor is operated under higher interaction regimes ($G = 0.7$ kg/m^{2}s), so did the relative errors became larger.

The pressure drop predictions were plotted in Figure 11 as a function of liquid flow rate and modifying also the gas flow rate from 0.1 to 0.7 kg/m^{2}s at $P = 30$ bar. The calculated relative error between the computed and experimental[1,34] two-phase pressure drop was found to be smaller than those obtained with the liquid holdup simulations at $G = 0.7$ kg/m^{2}s. At the lowest liquid flow rate, the pressure drop relative error moved from 8.4 to 16.2% as the gas flow rate increased from 0.1 to 0.7 kg/m^{2}s. Moreover, in the opposite extreme

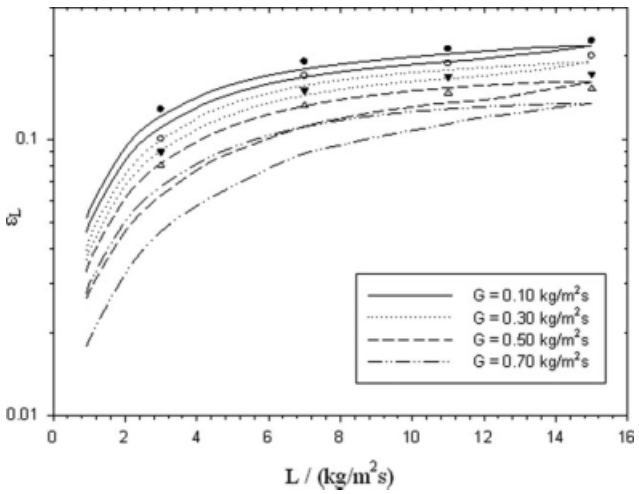

Figure 10. Effect of gas flow rate on liquid holdup predictions as a function of liquid flow rate (HRIC, time step = 10^{-5} s, 10^6 of tetrahedral cells, G = 0.1 kg/m^{2}s, P = 30 bar, d_p = 2 mm and experimental data from Nemec and Levec, 2005).[34]

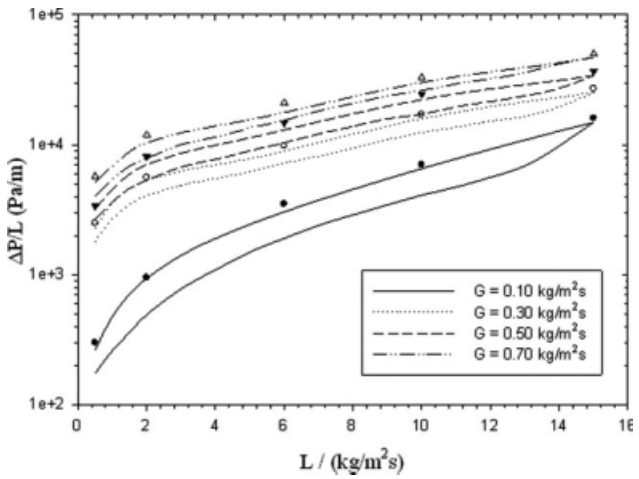

Figure 11. Effect of gas flow rate on two-phase pressure drop predictions as a function of liquid flow rate (HRIC, time step = 10^{-5} s, 10^6 of tetrahedral cells, G = 0.1 kg/m^{2}s, P = 30 bar, d_p = 2 mm and experimental data from Nemec and Levec, 2005).[34]

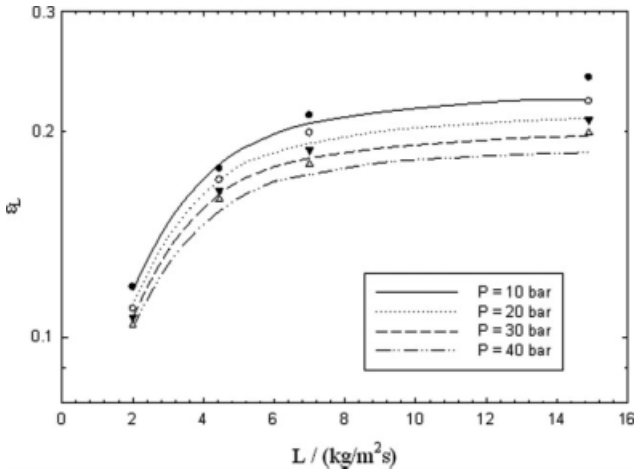

Figure 12. Effect of operating pressure on liquid holdup predictions as a function of liquid flow rate (HRIC, time step = 10^{-5} s, 10^6 of tetrahedral cells, G = 0.1 kg/m^{2}s, P = 30 bar, d_p = 2 mm and experimental data from Nemec and Levec, 2005).[34]

(high liquid flow rate $L = 15$ kg/m^{2}s) the pressure drop relative error became 7.7% at $G = 0.1$ kg/m^{2}s. Therefore, while the increase of liquid flow rate shortened the relative errors for either liquid holdup (Figure 10) or two-phase pressure drop (Figure 11), the relative errors were found to be directly proportional to the increase of gas flow rate.

Figure 12 shows the liquid holdup predictions as a function of liquid flow rate at different operating pressures. As one can observe, the higher the liquid flow rate was, the larger deviation between the liquid holdup experimental data and computed results was found. The liquid holdup profiles at different pressures were qualitatively similar as those obtained in the evaluation of gas flow rate in Figure 10. The effect of operating pressure on two-phase pressure drop as a function of liquid flow rate is shown in Figure 13. Once again, a higher pressure drop was obtained when increasing the operating pressure up to 40 bar. Indeed, the VOF model exhibited consistent behavior for the whole range of simulated liquid flow rate demonstrating that the lower relative errors were obtained at lower interaction regimes.

Catalyst wetting

As pilot and bench-scale trickle-bed reactors are generally operated at the same liquid hourly space velocities as the commercial-scale reactors, inefficient catalyst wetting has been reported at relatively low liquid superficial velocities. The VOF model was then used to evaluate this hydrodynamic performance parameter that is often related with the low utilization degree of the catalyst packing preventing optimum reactant conversions and product selectivities. Since the HRIC scheme gave discretization scheme-independent CFD results for both liquid holdup and two-phase pressure, it was used to compute the average and local catalyst wetting efficiency in the trickle-bed reactor with the finest mesh and with a time step of 10^{-5} s.

Figure 14a shows a semicylindrical slice made inside the catalytic bed at $L = 1$ kg/m^{2}s, $G = 0.1$ kg/m^{2}s, $P = 30$ bar. The orientation is given by the orthogonal axes shown adjacent to the 3D slice. This 3D visualization of trickle flow shows two distinct regions of liquid holdup: liquid rivulets characterized by their relatively large cross-sectional area and surface liquid seen as thin layers on the solid surfaces. The rivulet formation has been identified experimentally by means of magnetic resonance imaging. to gain insight how the individual rivulets develops, Figure 14b shows the same semi-cylindrical slice increasing the liquid flow rate up to 15 kg/m^{2}s at $G = 0.1$ kg/m^{2}s, $P = 30$ bar. As one can observe, the catalytic bed became more flooded with liquid and the overall wetting efficiency was enhanced due to the better axial and radial liquid distribution. This procedure was then used to determine the catalyst surface area that was filled with liquid as a function of liquid flow rate and how the wetting efficiency of individual catalyst particles was influenced by the local structure of the TBR packing.

In Figures 15a–e, successive radial planes was presented at $L = 1$ kg/m^{2}s, $G = 0.1$ kg/m^{2}s, $P = 30$ bar for the liquid phase along the catalytic bed at the second, forth, sixth, eighth, ninth, and tenth axial catalytic layers. As it can be seen, the outer contours of these slicing planes for each catalytic layer began with a well-defined circumferential profile for the corresponding spherical particles. At the second catalytic layer, it is possible to identify by the projection profiles obtained in the void-space that the liquid flows preferentially through the void spaces. Following the vertical downwards direction, the liquid stream is pushed against the catalyst particle by the gas phase. One of the driving forces acting on the liquid phase is the drag force at the gas-liquid interface which is a function of gas velocity which reduces the amount of liquid held in the void-space of the catalytic bed. Hence, the liquid retained in the void-space is expelled more vigorously by the gas superficial velocity resulting in the outer and contiguous profiles shown from the forth and sixth

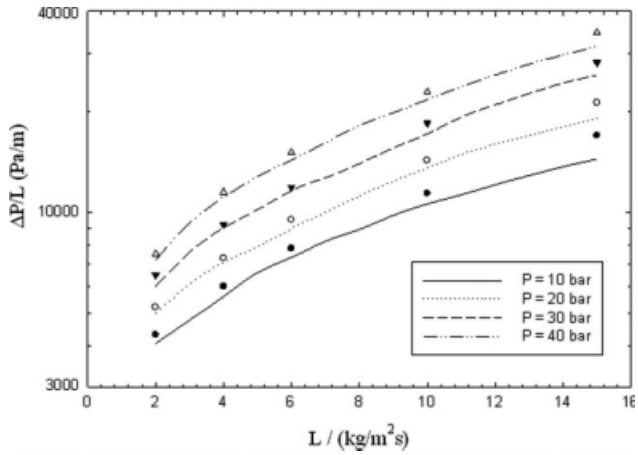

Figure 13. Effect of operating pressure on two-phase pressure drop predictions as a function of liquid flow rate (HRIC, time step = 10^{-5} s, 10^6 of tetrahedral cells, G = 0.1 kg/m^{2}s, P = 30 bar, d_p = 2 mm and experimental data from Nemec and Levec, 2005).[34]

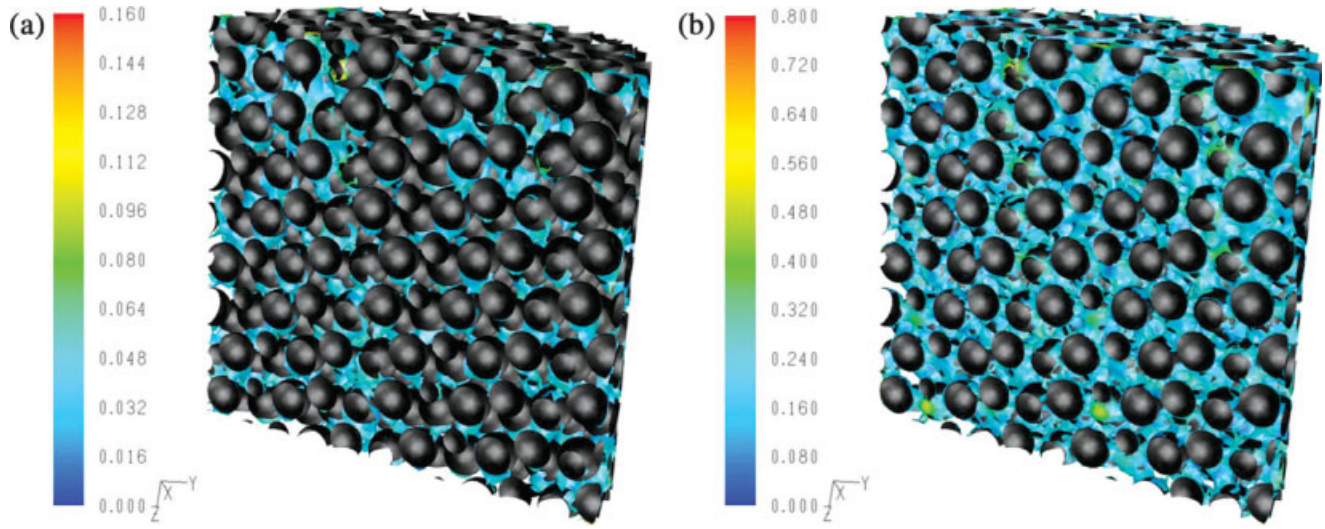

Figure 14. (a) Semicylindrical slice made inside the catalytic bed at L = 1 kg/m^{2}s and (b) L = 15 kg/m^{2}s, G = 0.1 kg/m^{2}s, P = 30 bar.

[Color figure can be viewed in the online issue, which is available at www.interscience.wiley.com.]

catalytic layers onwards. This was an expected behavior since the gas flow rate if often adjusted to improve the wetting efficiency due to the improved spreading of the liquid holdup over the external packing area. Moreover, the effect of gas flow rate on the wetting efficiency and liquid holdup is more pronounced at elevated pressure as reported by several authors.[1,2,4] This axial evolution of wetting efficiency at different cross-sections demonstrates that as long the liquid flows throughout the catalytic bed the liquid phase is spreading out of films on the catalyst particle by surface tension effect. It is worthwhile to mention that the calculation of surface tension effects on triangular and tetrahedral meshes

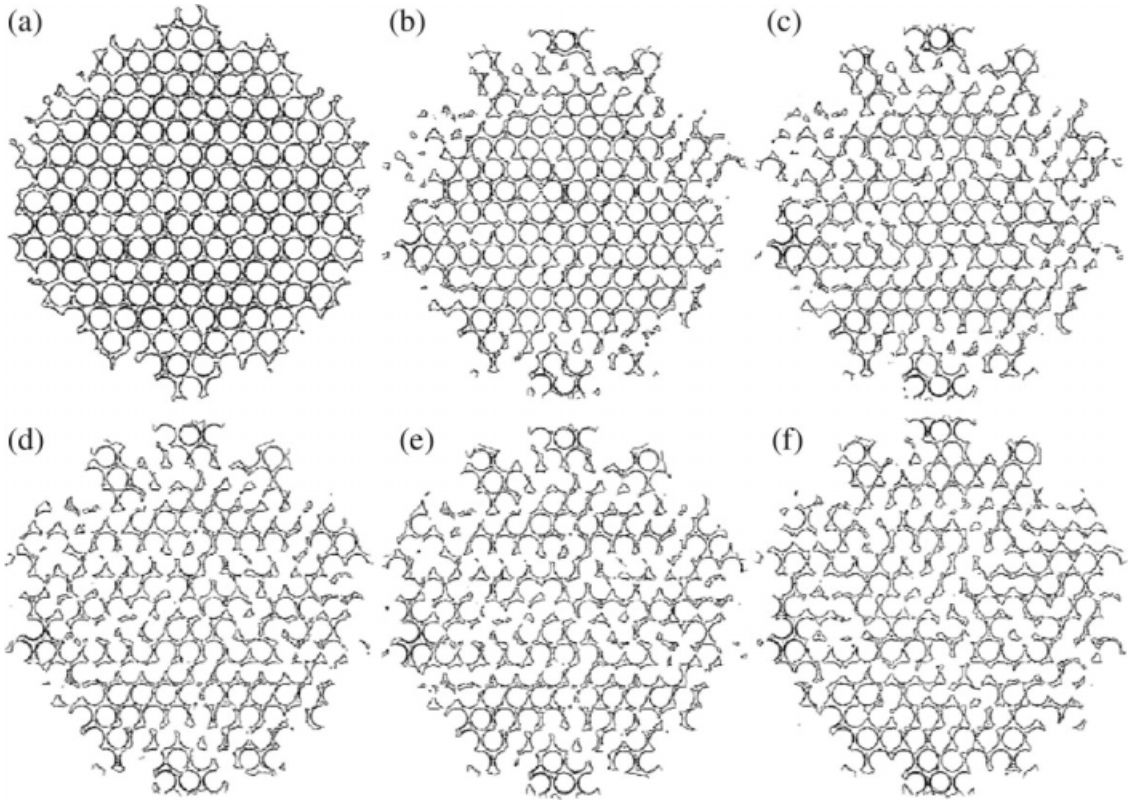

Figure 15. (a–f) Radial planes of the catalytic bed at different cross-sections for the 2nd, 4th, 6th, 8th, 9th, and 10th axial catalytic layers shown in Figure1 (HRIC, time step = 10^{-5} s, 10^6 of tetrahedral cells, L = 1 kg/m^{2}s, G = 0.1 kg/m^{2}s, P = 30 bar, d_p = 2 mm).

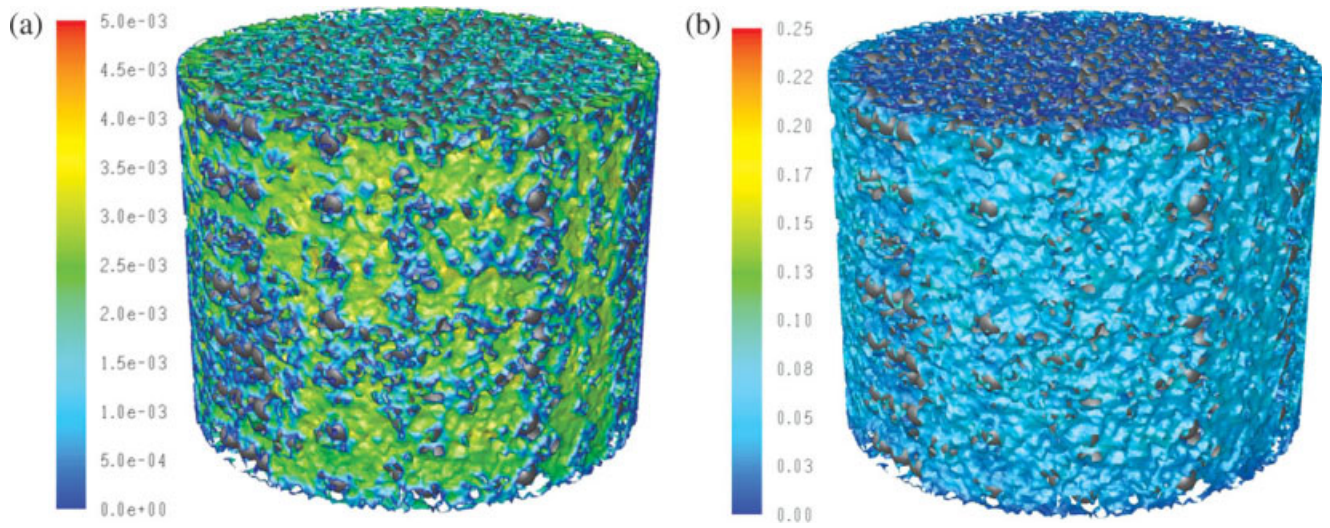

Figure 16. (a) Instantaneous snapshot of liquid holdup isosurface (ε_L = 0.06) colored by liquid velocity magnitude and (b) colored by the computed dimensionless Courant number (HRIC, time step = 10^{-5} s, 10^6 of tetrahedral cells, L = 1 kg/m^{2}s, G = 0.1 kg/m^{2}s, P = 30 bar, d_p = 2 mm).

[Color figure can be viewed in the online issue, which is available at www.interscience.wiley.com.]

is not as accurate as on quadrilateral and hexahedral meshes according to FLUENT documentation. However, the hydrodynamic validation accomplished in Figures 2 and 3 did not revealed any significant impact of the tetrahedral mesh choice for mesh-independent results. According to Figure 15a, it is clear that at the second layer the catalyst particle does not adsorb the liquid phase as Figure 15b shows at forth layer. As one moves along the catalytic bed, the liquid phase is better adsorbed by the catalyst particle and further enhancing the wetting efficiency. At the tenth catalytic layer, Figure 15f shows that the liquid phase filled the void-space between the catalyst particles with a higher extension when comparing with earlier radial planes for the liquid volume fraction (i.e., Figure 15a) and consequently the gas phase flows around the existent gap left after the adsorption of liquid phase on the spherical particle. The average wetting efficiency computed with the VOF model at the final cross-section (10th catalytic layer) was about 82%. It should be pointed out that in the CFD simulations, the boundary conditions at the TBR inlet specified a homogeneous distribution of the liquid flow which guarantees at least a better liquid distribution in the reactor and reduces possible radial heterogeneities of wetting efficiency even at lower superficial liquid velocities (L = 1 kg/m^{2}s).

At L = 1 kg/m^{2}s, G = 0.1 kg/m^{2}s, P = 30 bar, an instantaneous snapshot of a liquid holdup isosurface (ε_L = 0.06) colored by velocity magnitude values is shown in Figure 16a whereas in Figure 16b the same instantaneous liquid holdup snapshot was colored by the value of Courant number defined in Eq. 20. The Courant number distribution map ($N_c \approx 0.05$) in Figure 16b showed that the CFL condition was always met during the VOF calculations. This computational domain is located in the axial and radial TBR centre so that it can be assumed that inlet flow effects can be neglected throughout the entire VOF hydrodynamic simulation. According to Figure 16a, with an average value of about 0.003 cm/s, the axial evolution of wetting efficiency addressed in Figures 15a–e was found to confirm the qualitative radial profiles for the liquid distribution around the catalyst particle and its relationship with the superficial liquid velocities. At high-pressure operation, the liquid holdup isosurface revealed spatially the existence of relevant dry zones formed in the packed bed and confirmed the channeling phenomena typically encountered in lower interaction regimes that is often identified as the main cause of poor hydrodynamic and reaction performance of trickle-bed reactors.

Conclusions

A high-pressure trickle-bed reactor was modeled by means of a Volume-of-Fluid CFD model. The numerical simulations were evaluated quantitatively by experimental data from the literature. During grid optimization and validation, the effects of mesh size, time step and convergence criteria were evaluated plotting the hydrodynamic predictions as a function of liquid flow rate. Several discretization methods for the volume fraction equation were investigated including Quadratic Upwind Interpolation for Convective Kinematics, Geometric Reconstruction, Compressive Interface Capturing Scheme for Arbitrary Meshes and High-Resolution Interface Capturing schemes. High-order differencing schemes were found to give better computed results for either liquid holdup or two-phase pressure drop.

After ascertain mesh size, time step and differencing scheme independent CFD results, the VOF model was used to evaluate the effect of gas flow rate on hydrodynamics demonstrating its considerable influence on the liquid holdup in the range G = 0.1–0.7 kg/m^{2}s. Finally, the multiphase model was to compute radial planes of liquid volume fraction at different axial locations for the packed bed. It was found that wetting efficiency can be captured by VOF model and as long as the fluid phases moves through the catalytic bed, so do the catalyst wetting is improved considerably. During the VOF simulations, it was also verified that the

dimensionless Courant number was always below than 0.25 according to the Courant-Friedrichs-Lewy condition.

Acknowledgements

The authors gratefully acknowledge the financial support of REMOVALS—6th Framework Program for Research and Technological Development, FP06 Project no. 018525 and Fundação para a Ciência e Tecnologia, Portugal.

Notation

C_μ, $C_{1\varepsilon}$, $C_{2\varepsilon}$ = k-ε model parameters: 0.09, 1.44, 1.92
d_p = catalyst particle nominal diameter, m
$\vec{g}$ = gravitational acceleration, 9.81m/s^2
G = gas mass flux, kg/m^{2}s
G_k = generation rate of turbulent kinetic energy
k = k-ε model kinetic energy
k_{eff} = effective thermal conductivity
L = liquid mass flux, kg/m^{2}s
p = $p$ressure, bar
Re_i = Reynolds number based on intersticial velocity [Re/ε]
S_i = source mass for phase i, ppm
t = time, s
$\vec{u}$ = superficial vector velocity, m/s
x = Cartesian coordinate, m

Greek letters

α_i = volume fraction of ith phase
ε = k-ε model dissipation energy
κ = gas–liquid interface curvature
ρ_i = density of ith phase, kg/m^3
Δp = total pressure drop, Pa
σ = surface tension, N m
σ_k, σ_ε = k-ε model parameters: 1.2, 1.0
τ = residence time, s
$\overline{\overline{\tau_i}}$ = shear stress tensor of ith phase, Pa
μ_i = viscosity of ith phase, Pa s

Subscripts

G = Gas phase
i = ith phase
L = liquid phase
S = solid phase

Literature Cited

1. Al-Dahhan MH, Larachi F, Dudukovic MP, Laurent A. High pressure trickle-bed reactors: a review. *Ind Eng Chem Res.* 1997;36:3292–3314.
2. Dudukovic MP, Larachi F, Mills PL. Multiphase catalytic reactors: a perspective on current knowledge and future trends. *Catal Rev Sci Eng.* 2002;44:123–246.
3. Jiang Y, Khadilkar MR, Al-Dahhan MH, Dudukovic MP. CFD modeling of multiphase flow distribution in catalytic packed bed reactors: scale down issues. *AIChE J.* 2002;48:716–730.
4. Gunjal PR, Kashid MN, Ranade VV, Chaudhari RV. Hydrodynamics of trickle-bed reactors: experiments and CFD modeling. *Ind Eng Chem Res.* 2005;44:6278–6294.
5. Nigam KDP, Larachi F. Process intensification in trickle-bed reactors. *Chem Eng Sci.* 2005;60:5880–5894.
6. Saroha AK, Indraneel N. Pressure drop hysteresis in trickle bed reactors. *Chem Eng Sci.* 2008;63:3114–3119.
7. Kothe DB. Perspective on Eulerian finite volume methods for incompressible interfacial flows. In: *Free Surface Flows*. New York: Springer-Verlag, 1998:267–331.
8. Crooks R, Whitez JC, Boger DV. The role of dynamics surface tension and elasticity on the dynamics of drop impact. *Chem Eng Sci.* 2001;56:5575–5592.
9. Scheller BL, Bousfield DW. Newtonian drop impact with solid surface. *AIChE J.* 1995;41:1357–1367.
10. Ted M, Kuhn DCS, Tran H. Spread and rebound of liquid droplets upon impact on flat surfaces. *AIChE J.* 1997;43:2169–2179.
11. Yuan MH, Yang YH, Li TS, Hu ZH. Numerical simulation of film boiling on a sphere with a volume of fluid interface tracking method. *Int J Heat Mass Transf.* 2008;51:1646–1657.
12. Glatzel T, Litterst C, Cupelli C, Lindemann T, Moosmann C, Niekrawietz R, Streule W, Zengerle R, Koltay P. Computational fluid dynamics (CFD) software tools for microfluidic applications—a case study. *Comput Fluids.* 2008;37:218–235.
13. Gopala VR, van Wachem BGM. Volume of fluid methods for immiscible-fluid and free-surface flows. *Chem Eng J.* 2008;141:204–221.
14. Morel C. Modeling approaches for strongly non-homogeneous two-phase flows. *Nucl Eng Des.* 2007;237:1107–1127.
15. Heggemann M, Hirschberg S, Spiegel L, Bachmann C. CFD simulation and experimental validation of fluid flow in liquid distributors. *Chem Eng Res Des.* 2007;85:59–64.
16. Sáez AE, Carbonell RG. Hydrodynamic parameters for gas liquid cocurrent flow in packed beds. *AIChE J.* 1985;31:52–62.
17. Herskowitz M, Smith JM. Trickle Bed reactors: a review. *AIChE J.* 1983;29:1–18.
18. Kan KM, Greenfield PF. Multiple hydrodynamic states in cocurrent two phase down flow through packed beds. *Ind Eng Chem Process Des Dev.* 1978;17:482.
19. Kan KM, Greenfield PF. Pressure drop and hold up in two phase cocurrent trickle flows through beds of small particles. *Ind Eng Chem Process Des Dev.* 1979;18:740–745.
20. Christensen G, Sundaresan S, McGovern SJ. Cocurrent downflow of air and water in a two-dimensional packed column. *AIChE J.* 1986;32:1677–1689.
21. Levec J, Grosser K, Carbonell RG. The hysteretic behavior of pressure drop and liquid hold up in trickle beds. *AIChE J.* 1988;34:1027–1030.
22. Levec J, Grosser K, Carbonell RG. The hydrodynamics of trickling flow in packed beds, Part 2: experimental observations. *AIChE J.* 1986;32:369–380.
23. Rode S, Midoux N, Latifi MA, Storck A. Multiple hydrodynamic states in trickle beds operating in high interaction regimes: liquid saturation and flow regime transitions. *Chem Eng Sci.* 1994;49:2535–2540.
24. Ravindra PV, Rao DP, Rao MS. Liquid flow texture in trickle bed reactors: an experimental study. *Ind Eng Chem Res.* 1997;36:5133–5145.
25. Melli TR, Scriven LE. Theory of two phase cocurrent downflow in networks of passages. *Ind Eng Chem Res.* 1991;30:951–969.
26. Gunjal PR, Ranade VV, Chaudhari RV. Computational study of a single-phase flow in packed beds of spheres. *AIChE J.* 2005;51:365–378.
27. Brackbill J, Kothe D, Zemach C. A continuum method for modelling surface tension. *J Comput Phys.* 1992;100:335–354.
28. Dybbs A, Edwards RV. Fundamentals of Transport Phenomena in Porous Media (Bear J, Corapcioglu M, editors). Dordrecht: Martins Nijhoff, 1984.
29. Elghobashi S, Abou-Arab T, Rizk M, Mostafa A. Prediction of the particle-laden jet with a two-equation turbulence model. *Int J Multiphase Flow.* 1984;10:697–710.
30. FLUENT 6.1. User's Manual to FLUENT 6.1. Fluent Inc., Centrera Resource Park, 10 Cavendish Court, Lebanon, USA, 2005.
31. Lopes RJG, Quinta-Ferreira RM. Trickle-Bed CFD. Studies in the catalytic wet oxidation of phenolic acids. *Chem Eng Sci.* 2007;62:7045–7052.
32. Nijemeisland M, Dixon AG. Comparison of CFD simulations to experiment for convective heat transfer in a gas-solid fixed bed. *Chem Eng J.* 2001;82:231–246.
33. GAMBIT 2. User's Manual to GAMBIT 2. Fluent Inc., Centrera Resource Park, 10 Cavendish Court, Lebanon, USA, 2005.
34. Nemec D, Levec J. Flow through packed bed reactors: 2, Two phase concurrent downflow. *Chem Eng Sci.* 2005;60:6958–6970.
35. Ubbink O, Issa RI. Method for Capturing sharp fluid interfaces on arbitrary meshes. *J Comput Phys.* 1999;153:26–50.
36. Muzaferija S, Peric M, Sames P, Schelin T. A two-fluid Navier-Stokes solver to simulate water entry. In: *Proceedings of 22nd Twenty-Second Symposium on Naval Hydrodynamics*. Washington, DC: National Academy Press, 1999:638–651.
37. Hirt CW, Nichols BD. Volume of fluid (VOF) method for the dynamics of free boundaries. *J Comput Phys.* 1981;39:201–225.
38. Leonard BP. The ULTIMATE conservative difference scheme applied to unsteady one-dimensional advection. *Comp Methods Appl Mech Eng.* 1991;88:17–74.

Appendix

VOF Differencing Schemes of Volume Fraction Equation

Geometric reconstruction scheme. In the geometric reconstruction approach, the standard interpolation schemes that are used in FLUENT are used to obtain the face fluxes whenever a cell is completely filled with one phase or another. When the cell is near the interface between two phases, the geometric reconstruction scheme is used. The geometric reconstruction scheme represents the interface between fluids using a piecewise-linear approach. It assumes that the interface between two fluids has a linear slope within each cell, and uses this linear shape for calculation of the advection of fluid through the cell faces. The first step in this reconstruction scheme is calculating the position of the linear interface relative to the center of each partially-filled cell, based on information about the volume fraction and its derivatives in the cell. The second step is calculating the advecting amount of fluid through each face using the computed linear interface representation and information about the normal and tangential velocity distribution on the face. The third step is calculating the volume fraction in each cell using the balance of fluxes calculated during the previous step.

Donor-acceptor scheme. In the donor-acceptor approach, the standard interpolation schemes that are used in FLUENT are used to obtain the face fluxes whenever a cell is completely filled with one phase or another. When the cell is near the interface between two phases, a "donor-acceptor" scheme is used to determine the amount of fluid advected through the face.[37] This scheme identifies one cell as a donor of an amount of fluid from one phase and another (neighbor) cell as the acceptor of that same amount of fluid, and is used to prevent numerical diffusion at the interface. The amount of fluid from one phase that can be convected across a cell boundary is limited by the minimum of two values: the filled volume in the donor cell or the free volume in the acceptor cell. The orientation of the interface is also used in determining the face fluxes. The interface orientation is either horizontal or vertical, depending on the direction of the volume fraction gradient of the qth phase within the cell, and that of the neighbor cell that shares the face in question. Depending on the interface's orientation as well as its motion, flux values are obtained by pure upwinding, pure downwinding, or some combination of the two.

Compressive interface capturing scheme for arbitrary meshes scheme. The compressive interface capturing scheme for arbitrary meshes (CICSAM), based on the Ubbink's work,[35] is a high-resolution differencing scheme. The CICSAM scheme is particularly suitable for flows with high ratios of viscosities between the phases. CICSAM is implemented in FLUENT as an explicit scheme and offers the advantage of producing an interface that is almost as sharp as the geometric reconstruction scheme.

Modified high-resolution interface capturing scheme. For simulations using the VOF multiphase model, upwind schemes are generally unsuitable for interface tracking because of their overly diffusive nature. Central differencing schemes, while generally able to retain the sharpness of the interface, are unbounded and often give unphysical results. To overcome these deficiencies, FLUENT uses a modified version of the High-Resolution Interface Capturing scheme. The modified HRIC scheme is a composite NVD scheme that consists of a nonlinear blend of upwind and downwind differencing.[36]

First, the normalized cell value of volume fraction, $\tilde{\phi}_c$, is computed and is used to find the normalized face value, $\tilde{\phi}_f$, as expressed in Eq. A1:

$$\tilde{\phi}_c = \frac{\phi_D - \phi_U}{\phi_A - \phi_U} \tag{A1}$$

where A is the acceptor cell, D is the donor cell, and U is the upwind cell, and:

$$\tilde{\phi}_f = \begin{cases} \tilde{\phi}_c & \tilde{\phi}_c < 0 \text{ or } \tilde{\phi}_c > 1 \\ 2\tilde{\phi}_c & 0 \le \tilde{\phi}_c \le 0.5 \\ 1 & 0.5 \le \tilde{\phi}_c \le 1 \end{cases} \tag{A2}$$

Here, if the upwind cell is not available (e.g., unstructured mesh), an extrapolated value is used for $\tilde{\phi}_U$. Directly using this value of $\tilde{\phi}_f$ causes wrinkles in the interface, if the flow is parallel to the interface. So, FLUENT switches to ULTIMATE QUICKEST scheme (the one-dimensional bounded version of the QUICK scheme[38]) based on the angle between the face normal and interface normal:

$$\phi_f^{\tilde{U}Q} = \begin{cases} \tilde{\phi}_c & \tilde{\phi}_c < 0 \text{ or } \tilde{\phi}_c > 1 \\ \text{MIN}\left(\tilde{\phi}_f, \frac{6\tilde{\phi}_c+3}{8}\right) & 0.5 \le \tilde{\phi}_c \le 1 \end{cases} \tag{A3}$$

This leads to a corrected version of the face volume fraction, $\tilde{\phi}_f^*$:

$$\tilde{\phi}_f^* = \tilde{\phi}_f \sqrt{\cos\theta} + \left(1 - \sqrt{\cos\theta}\right)\phi_f^{\tilde{U}Q} \tag{A4}$$

where

$$\cos\theta = \frac{\nabla\phi \cdot \vec{d}}{|\nabla\phi|\left|\vec{d}\right|} \tag{A5}$$

and $\vec{d}$ is a vector connecting cell centers adjacent to the face f.

The face volume fraction is now obtained from the normalized value computed above as expressed in Eq. (A6):

$$\tilde{\phi}_f = \tilde{\phi}_f^*(\phi_A - \phi_U) + \phi_U \tag{A6}$$

The modified HRIC scheme provides improved accuracy for VOF calculations when compared to QUICK and second-order schemes, and is less computationally expensive than the Geo-Reconstruct scheme.

Manuscript received Aug. 4, 2008, and revision received Jan. 21, 2009.